PCCP

Accepted Manuscript

ROYAL SOCIETY OF CHEMISTRY

www.rsc.org/pccp

Physical Chemistry Chemical Physics

RSCPublishing

ARTICLE

Transition Metal Selenides as Efficient Counter Electrode Materials for Dye-sensitized Solar Cells

Jiahao Guo,‡[a,b] Suxia Liang,‡[a] Yantao Shi,[a,*] Ce Hao,[a] Xuchun Wang,[b] and Tingli Ma[c,d*]

Cite this: DOI: 10.1039/x0xx00000x

Received 00th January 2012,
Accepted 00th January 2012

DOI: 10.1039/x0xx00000x

www.rsc.org/

Exploiting an alternative of the Pt-based counter electrode materials for triiodide reduction reaction has become a major interest in the fundamental research of dye-sensitized solar cells. Transition-metal selenides have recently been demonstrated as a promising non-precious metal electrocatalysts for triiodide reduction reaction. Herein, we prepared a series of transition-metal selenides via a free-reductant solvothermal method and used them as counter electrodes in high efficiency dye-sensitized solar cells. The electrochemical results showed that these selenides had excellent catalytic activity for the reduction of triiodine/iodine couple, and, except for $MoSe_2$, the conversion efficiencies of corresponding dye-sensitized solar cells were comparable to the sputtered Pt counter electrode. Theoretical investigation clearly revealed that the unsatisfactory performance of $MoSe_2$ mainly originated from the processes of adsorption and charge-transfer. These findings can help to better understand the electrocatalytic processes and thus offer some useful guidelines to develop more efficient electrochemical catalysts.

1. Introduction

Dye-sensitized solar cells (DSCs) are a typical third-generation photovoltaic device with mesoporous architecture and some attractive features, such as cost effectiveness, environmentally friendly, easy processing, and relatively high power conversion efficiency (PCE).[1] Over the past two decades, DSCs have been intensively studied to improve their photovoltaic performance and reduce production cost.[2] Among the basic components of DSCs is the counter electrode (CE), which has two important roles: to collect electrons from the external circuit; and to transfer the electrons to recycle the redox species of the redox couple (I_3^-/I^-) through catalytic reduction. Thus, the nature of CE is important in determining the photovoltaic performance of DSCs. Superior CE catalysts possess high electrocatalytic activity, good electrical conductivity, and chemical stability.[3] Based on these standards, platinum is a noble metal that has been widely used to fabricate efficient CE in DSCs, such as that of sputtering Pt, or pyrolytic Pt. Nevertheless, the high cost, limited resources, and corrosion by iodine species in electrolyte solution seriously restrict the large-scale application of Pt-based CEs in DSCs.[2a] Therefore, economic, stable, and effective non-Pt catalysts should be exploited to fabricate novel CEs.

Recently, our group has developed some inorganics compounds, such as oxides,[4] nitrides,[5] carbides,[6] sulfides,[7] phosphides,[8] and tellurides,[9] for fabrication of non-Pt CEs. As emerging functional materials, transition-metal selenides (TMSs) have drawn much interest because of their excellent semiconductor properties, photoelectric effects, and nonlinear optical characteristics. TMSs have been widely studied in the field of luminescence, display, infrared detectors, and photocatalysis.[10] TMSs also possess unique electrical properties, interesting chemical behaviour, and good chemical stability,[11] which are suitable for use as electrocatalysts. Despite being used for oxygen reduction reaction in fuel cells,[12] TMSs have been applied as CEs in DSCs only two years ago.[13] For DSCs, TMS-CEs are comparable with conventional Pt-CEs in terms of conversion efficiency. For example, $Co_{0.85}Se$, $Ni_{0.85}Se$ and $NiSe_2$ are synthesized via hydrothermal route in situ on FTO substrates and used directly as CEs in DSCs by Gong et al, in which high PCEs are obtained, even better than Pt-CE.[13a,b] In 2013, our group reported the superior catalytic activity of $NbSe_2$ with different nanostructures that were prepared through a facile and reductant-free solvothermal approach. The $NbSe_2$-based CEs also demonstrated a comparable performance to Pt-CE in DSCs.[13c] Although TMSs are suitable for use as CE materials and can significantly replace Pt in DSCs, the origin of high electrocatalytic activity of TMSs remains unclear. Only a few reports have provided theoretical investigation on the electrocatalytic behaviours of TMSs as CEs in DSCs.

In the current study, to research the catalytic regularity, we designed and synthesized three TMSs ($MoSe_2$, WSe_2, and $TaSe_2$) with similar crystal structures through a reductant-free solvothermal route. The crystal structures, morphologies, and electrocatalytic behaviour of the three TMSs were characterized. As CEs, WSe_2 and $TaSe_2$ exhibited higher electrocatalytic activities and better performance than $MoSe_2$, and PCEs of their corresponding DSCs nearly approached that of the DSCs with Pt-CE. Theoretical discussions on the electrocatalytic activity were performed based on the density functional theory (DFT). The unsatisfactory performance of $MoSe_2$ mainly originated from the processes of adsorption and charge transfer. Our experimental and theoretical results provide helpful information in understanding the electrocatalytic processes and offer some useful guidelines to develop more efficient CEs in DSCs.

2. Experimental

2.1 Materials preparation

TMSs nanostructure were synthesized via the method reported by our group,[13c] metal chlorides were used as metal precursors and Se powder was used as the selenium source. As an example, for WSe_2, in a typical procedure, WCl_6 and Se powder (molar ratio of 1:2) were mixed and added into moderate oleylamine (OLA) degassed with N_2 at room temperature. Subsequently the reaction mixture was transferred into a three-neck round-bottom flask, sealed, and degassed with high pure N_2 atmosphere under magnetic stirring and heated to be reacted for 4 h at 280 ^oC in N_2 atmosphere with vigorously agitation. Finally, the mixture was cooled slowly down to room temperature with an appropriate speed, and black products were obtained. Large amount of hexane were then added into the crude solution and theproducts were isolated by centrifugation repeatedly, dried under vacuum, and heated at 450 ^oC for 3h under N_2 atmosphere.

2.2 Preparation of TMSs counter electrodes and cell fabrication

A 12 μm thick TiO_2 film (P25, Degussa, Germany) was loaded on FTO glass by a screen-printing technique, sensitized with N719 dye (Solaronix SA, Aubonne, Switzerland) and used as the photoanode. The TMSs counter electrodes were fabricated with spray-coating technique as follow. 200 mg of the as-prepared TMSs were dispersed in 4 mL isopropanol and milled with a star ball mill (QM-QX04, Nanjing NanDa Instrument Plant) for 4 h and the slurry for spraying were obtained. The prepared slurry was sprayed onto FTO glass substrate (Asahi Glass, type-U, 14 Ω sq^{-1}, Japan) with an air brush (TD-128, Tiandi Co., Ltd.) connected to a mini compressor. The thickness of selenides CEs was around 8μm. Subsequently, the FTO glass coated with various pastes was then sintered under a N_2 atmosphere at 500 °C for 30 min in a tube furnace and the CEs were prepared. The Pt CE was prepared in according with the procedure in our previous work.[14] A DSCs device was fabricated with a photoanode, a counter electrode and a redox electrolyte. The redox electrolyte contained 0.06 M LiI, 0.6 M 1-butyl-3-methylimidazolium iodide, 0.03 M I_2, 0.5 M 4-tert-butyl pyridine, and 0.1 M guanidiniumthiocyanate in acetonitrile solution and injected into the interspace between the photoanode and counter electrode via capillary force. The two electrodes were sealed by double-faced insulated adhesive tapes. The active area of as-assembled DSCs was 0.16 cm^2. A symmetrical cell was assembled by sandwiching two identical CEs with the same electrolyte as used in the DSCs assembly. The as-assembled symmetrical cell was then subjected to electrochemical impedance spectroscopy and Tafel polarization measurement.

2.3 Characterizations of CE materials and DSCs

The X-ray powder diffraction (XRD) measurements of the synthesized selenide samples were measured using an automatic X-Ray powder diffractometer (D/Max 2400, Rigaku, Japan) with Cu Kαradiation (λ = 0.154 nm). The surface morphological characteristics and microstructure of the selenide samples were examined through field emission scanning electron microscopy (FESEM, FEI HITACHI S-4800) and transmission electron microscope (TEM, JEOJ-2010) with an acceleration voltage of 200 kV. Nitrogen adsorption isotherms were collected by a Tristar II 3020, Micromeritics adsorption analyzer at 77 K. Prior to adsorption measurements, the samples were degassed at 200 ^oC for at least 10 h. Pore size distributions (PSD) were calculated using the adsorption branch of the isotherms by Barrett-Joyner-Halenda (BJH) method; The total pore volume was estimated from the adsorption volume at a relative pressure (P/P_0) of 0.99. Cyclic voltammetry (CV) was carried out in a three-electrode system of an anhydrous acetonitrile solution containing 0.1 M $LiClO_4$, 10 mMLiI, and 1 mM I_2 at a scan rate of 10 mV s^{-1} using a CHI630D electrochemical workstation (Chenhua, Shanghai). The as-prepared selenide CEs was assigned as a working electrode; a Pt wire was utilized as a counter electrode; an Ag/AgCl electrode was used as a reference electrode. Electrochemical impedance spectroscopy (EIS) measurements were conducted using the dummy cell on a computer-controlled electrochemical workstation (Zennium Zahner, Germany) under dark conditions. The geometric active area of the symmetrical cell was 0.64 cm^2. The measured frequency ranged from 100 mHz to 1 MHz with a bias of −0.75 V and the AC amplitude of the alternating current was set at 10 mV. The obtained EIS data were analyzed using commercially available Z-view software and fitted in terms of an appropriate equivalent electric circuit. Tafel polarization measurements were employed an electrochemical workstation system (CHI630D, Chenhua, Shanghai). The scan rate was 10 mV·s^{-1}. The photovoltaic performance of the DSCs was evaluated by a Keithley digital source meter (Keithley 2601, USA) under simulated sunlight illumination conditions (Xe arc lamp, 1.5 AM, 100 mW cm^{-2}, PEC-L15, Peccell, Japan).

3. Computational Method

DFT computations were performed using projector augmented wave (PAW) potentials in the Vienna ab initio simulation package (VASP). [15-18] Relaxations were carried out using conjugate-gradient algorithm, and stopped if all forces were smaller than 0.01 eV/Å. LDA functionals are employed for $MoSe_2$, WSe_2, and $TaSe_2$ which were hexagonal crystal structure. The occupancy of the one-electron states was calculated using the Gaussian smearing (SIGMA = 0.1 eV). When band structure was calculated, the primitive cell of the three transition metal selenides was used. Brillouin-zone integrations were performed using Monkhorst-Pack grids of special points with 11×11×11 meshes. The kinetic-energy cutoff of plane wave was set to 345eV for $Cr_{5.6}Se_8$ and the other four selenides were set to 290 eV. The energy convergence was selected 1×10^{-5} eV/atom.

As shown in Figure S3, the fringe spacing was 0.282 nm and 0.283 nm which agreed well with the values for (100) lattice planes of hexagonal $MoSe_2$ and WSe_2. Considering that the mostly exposed surfaces were perpendicular to the surfaces which fringe spacing corresponding to, accordingly, $MoSe_2$ (001) and WSe_2 (001) surfaces were chosen as the computational model, which modeled as a p (2×2) periodic slab with 6 atomic layers and the vacuum between slabs was 20 Å. The atoms in the bottom layer were fixed, and all other atoms were fully relaxed. A corresponding 3×3×1 k-points mesh was applied during optimizations.

4. Results and discussion

4.1. Morphology and structure characterizations

The crystal structures of the as-obtained three samples were characterized by XRD analysis (Figure S1). First, all of the diffraction peaks in curves (a), (b), and (c) could be well designated to JCPDS Nos. 29-0914, 38-1388, and 19-1303, respectively, which were both identified as hexagonal crystal structures. The lattice parameters of the three samples are: a =3.287 Å and c=12.925 Å for $MoSe_2$, a=3.286 Å and c =12.983 Å for WSe_2, and a=3.436 Å and c=12.696 Å for $TaSe_2$, indicating that their crystal structures are almost similar. In general, diselenide (MSe_2) has layered structures, in which the metal ion possesses a six-coordinate trigonal-prismatic structure.[19] The XRD peak assignments of the three samples are shown in the Supporting Information. No impurity peak was observed in all of the XRD patterns (Figure S1).

The morphologies of the as-synthesized three TMSs were investigated by SEM and TEM (Figure 1 and Figures S2, S3). $MoSe_2$ is composed of interlaced and ultrathin nanosheets (Figure

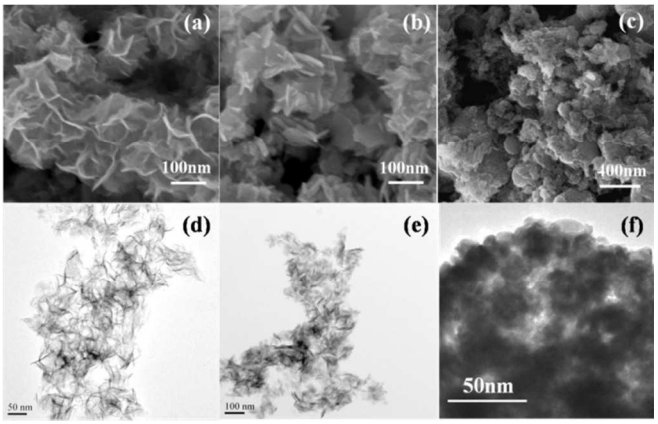

Figure 1 SEM and TEM images of the as-synthesized $MoSe_2$ (a) (d), WSe_2 (b) (e), and $TaSe_2$ (c) (f).

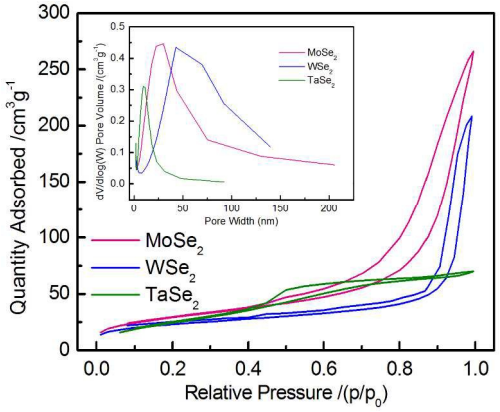

Figure 2 N_2 adsorption-desorption isotherms at 77 K. The inset is the pore-size distribution curves of three TMSs.

1a). The thickness of the $MoSe_2$ nanosheets is approximately 10 nm with typical lateral dimensions between 100 and 150 nm. The $MoSe_2$ nanosheets are also inclined to form connected spheres. Similar to $MoSe_2$, WSe_2 is composed of several interlaced nanoplates with an average thickness of approximately 15nm and width of between 60 and 100nm, which are slightly smaller than those of the $MoSe_2$ nanosheets (Figure1b). The structural advantages of the interlaced nanosheets or nanoplates are evident as they can offer a large specific area that can be accessed with ease by adsorbate; large specific is also favorable to desorption of the product. In these two nanostructures, the grain boundaries that hinder electron transport should be minimized. These structural advantages are desired with regard to enhancing electrocatalytic activity and have been proven by subsequent electrochemical and photovoltaic measurements. The SEM image for $TaSe_2$ illustrates that its dominant structures are fluffy nanoparticles with a very wide size distribution (Figure 1c). TEM images of three TMSs CE materials are given in Figure1d-f. $MoSe_2$ showed interconnected nanosheets. WSe_2 exhibited nanoplate connected each other. $TaSe_2$ showed irregular nanoparticle aggregates. The HRTEM images of $MoSe_2$, WSe_2, and $TaSe_2$ (Figure S3) show lattice fringes with spacing of 0.282 nm, 0.283 nm, and 0.291 nm, corresponding to the (100), (100), and (101) planes of hexagonal $MoSe_2$, WSe_2, and $TaSe_2$, respectively.

Nitrogen adsorption isotherms were measured to investigate the pore structure of the three as-prepared materials. The isotherms of all samples are type-IV with a distinct hysteresis loop at relative pressures (P/P_0) from 0.45 to 1.0 (Figure 2), suggesting the presence of mesopores in these materials. The pore size distribution (PSD) curve of WSe_2 is centred approximately 43 nm whereas that of $MoSe_2$ is centered at approximately 30 nm, which is larger than that of $TaSe_2$ (≈10 nm). The PSD results further confirm the mesoporous structure of the three materials (inset of Figure 2). The mesoporous architecture of WSe_2 can facilitate I_3^- adsorption and molecular transport during the catalytic reaction process. The Bruanauer–Emmett–Teller (BET) surface area and the total pore volume of WSe_2 was estimated to be 95.6 m^2g^{-1} and 0.32 cm^3g^{-1}, in contrast to those of $MoSe_2$ (104.4 m^2g^{-1} and 0.41 cm^3g^{-1}) and $TaSe_2$ (78.8 m^2g^{-1} and 0.14 cm^3g^{-1}). The difference of surface area and pore size distribution of catalytic materials caused the difference of adsorption properties for I_3^-/I^- system and show a change in the catalytic activity and electrochemical properties, which impacted the photoelectric performance of DSCs.

4.2 Electrochemical characterization of CEs

The electrochemical catalytic activities of the three TMS-CEs for I_3^- reduction were also evaluated by cyclic voltammetry (CV). For comparison, the CV characterization of Pt-CE was performed under the same conditions. Figure 3 shows the CV curves of I_3^-/I^- redox couples using different CEs. For each CE, two typical pairs of oxidation and reduction peaks can be resolved. The redox couple at lower potential peaks (between 0.2 and 0.4 V vs. Ag/AgCl) corresponds to the reaction of $I_3^-+2e^-\rightarrow 3I^-$, and the redox couple at higher potential peaks (between 0.6 and 0.9 V vs. Ag/AgCl) corresponds to the reaction of $3I_2+2e^-\rightarrow 2I_3^-$. According to the reaction of I_3^-/I^-, the cathodic peak current density (J_{pc1}) and the anodic peak current density (J_{pa1}) reflect the reduction of the I_3^- ions and the oxidation of the I^- ions, respectively. The peak-to-peak separation (E_{pp}) also corresponds to the reversibility of the redox reaction. As shown in Figure 3, the CV profile of the three TMS-CEs are similar to that of the Pt-CE, indicating that these TMS-CEs are as effective as Pt in catalyzing the reduction of I_3^- to I^-. For WSe_2 CE, the J_{pc1} is slightly higher than that of Pt-CE, and the cathodic peak potentials is similar to Pt, suggesting that I_3^- can be reduced more easily on WSe_2 CE. By contrast, for the $TaSe_2$ and $MoSe_2$ CEs, the cathodic peak potentials and J_{pc1} are generally lower than that of Pt-CE, indicating that the catalytic activity of these two TMS-CEs for the reduction of I_3^- is inferior to that of Pt. Among the four CEs, the reduction current density of $MoSe_2$ is the lowest. Considering the larger surface area, $MoSe_2$ has a relatively low catalytic activity. The three TMS-CEs also exhibit smaller E_{pp} than that of Pt, suggesting good reversibility of the redox reaction. The TMS-CEs have low onset oxidation potential and oxidation peak potential, that is, the overpotential of the I^- oxidation reaction is lower, indicating that the I^- ion is easy to be oxidized. Compared to $TaSe_2$ and $MoSe_2$, WSe_2 has a higher oxidation current density, suggesting that I^- has a fast oxidation rate on the surface of WSe_2. Thus, the catalytic activity of WSe_2 for the reduction of I_3^- and oxidation of I^- is comparable to Pt-CE and much better than $MoSe_2$-based CE. The electrochemical stability of CE material is of great significance in terms of further application in DSCs. In this work, by means of consecutive CV measurements, we elucidated the stability of our three TMS-based CEs in electrolyte solution. As can be seen in Figure S4, 50 CV curves coincide very well, indicating that our three TMS-based CEs have all good stability under practical working conditions.

To investigate the electrochemical characteristics of these three TMS-based CEs, electrochemical impedance spectroscopy (EIS) measurements were performed with the use of symmetric cells consisting of two identical electrodes sandwiching the electrolyte (CE//electrolyte//CE) under dark conditions. Figure 4 shows the Nyquist plots obtained at −0.75V bias. The equivalent circuit for fitting the resultant impedance spectra by Z-view software is shown in the inset of Figure 4. Detailed EIS parameters are summarized in

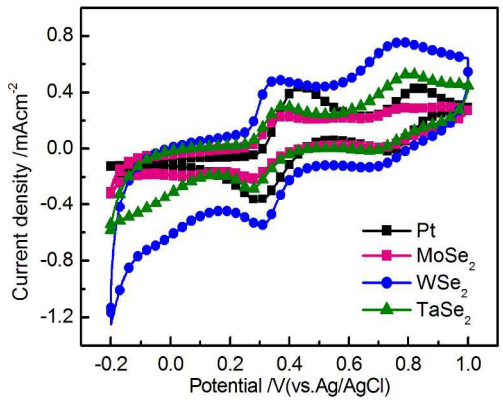

Figure 3 Cyclic voltammograms of triiodide/iodide redox couple for three TMSs and Pt CEs.

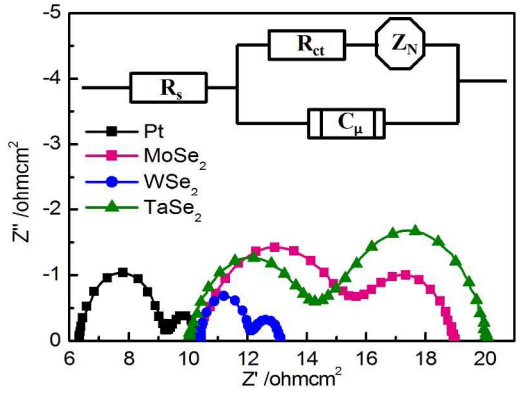

Figure 4 Nyquist plots of EIS for the symmetrical cells fabricated with two identical electrodes in I_3^-/I^-electrolyte system. The inset show the equivalent circuit of the symmetrical cells for Nyquist plot fitting.

Table1. Owing to the symmetric configuration of the dummy cell, the real R_{ct} was calculated as half of the value obtained from the Z-view fitting. The Nyquist plots illustrate the impedance characteristics, in which two semicircles can be observed at the high-frequency (left) and low-frequency (right) regions. The intercept on the real axis (Z' axis) at the high-frequency region represents the series resistance (R_s). The semicircle at the high-frequency regions arises from the charge-transfer resistance (R_{ct}) of the electrolyte/electrode interface, which reflects the electrocatalytic activity for I_3^- reduction in the electrolyte and the corresponding constant phaseelement (CPE). The second semicircle at the low-frequency region is derived from the Nernst diffusion impedance (Z_N) of I_3^-/I^- within the electrolyte. In contrast to Pt-CE, the larger R_s of the TMSs-based CEs can be observed. The R_s is mainly composed of the resistance of the FTO substrate, the bulk resistance of TMSs, and contact resistance, etc. The higher bulk resistance of TMSs and the worse adhesion between selenides and FTO substrate should be responsible for the higher R_s. The R_s values of three TMS-CEs were very close, indicating similar conductivity. Among the three TMS-based CEs, the R_s value of $TaSe_2$ was the minimum. On the basis of the diameters of the first semicircles and the fitted results (Table 1), the R_{ct} for the WSe_2-CE (0.78 Ωcm^2) is smaller than that of the Pt-CE (1.32 Ωcm^2), whereas those of the $TaSe_2$ (1.89 Ωcm^2) and $MoSe_2$ (2.43 Ωcm^2) CEs are larger than that of the Pt-CE. These results suggest that WSe_2 possesses superior electrocatalytic activity for I_3^- electrochemical reduction. Among the three TMS-CEs, WSe_2 and $MoSe_2$ demonstrate the higher CPE values, thereby indicating large contact surface area between the CE and electrolyte.[20] The ionic Z_N of WSe_2 is 1.15 Ωcm^2, which is lower than that of the other two CEs and close to that of Pt-CE, thereby suggesting larger apparent diffusion coefficient of I_3^- within this CEs. These findings could be attributed to the suitable pore structures of WSe_2. The conductivity of CE material is a important factor for the performance of DSCs. Conductivities of these three TMSe-CEs were characterized using linear sweep voltammetry by two counter electrodes, as reported previously.[21] As shown in Figure S5, the slopes of three curves decreases gradually according to the order of $TaSe_2$, $MoSe_2$, WSe_2, indicating the same change order of conductivity for our three TMS materials. This result is consistent with the changing rules of Rs.

To further elucidate the electrocatalytic activities, we measured the Tafel curves of the three TMSs and Pt-CEs using the dummy cells in the EIS experiments and the results show in Figure 5. As shown in Figure 5, the Tafel curve demonstrates the logarithmic current density (LogJ) as a function of the potential (V). The exchange current density, J_0 and the limiting diffusion current density (J_{lim}) related to the catalytic activity of the catalysts can be obtained from the Tafel curves. From Figure 5 and Table 1, WSe_2 CE exhibit a large slope compared with Pt-CE, indicating a high J_0. This result proves that WSe_2 CE has high catalytic activity for the reduction of I_3^- to I^-. Similar to WSe_2, $TaSe_2$-based CE also shows a considerable catalytic activity. However, in the case of $MoSe_2$-based CE, the gentle slope shows a relatively lower catalytic activity. J_0 can also be calculated by Equation 1, where R is the gas constant, F is the Faraday constant, T is the temperature, and *n* is the number of electrons in the reduction of I_3^- at the electrolyte/CE interface. Combined with the corresponding EIS results, the change tendency of J_0 on the three TMS-CEs are generally consistent with the overall Tafel-polarization measurements.

$$J_0 = \frac{RT}{nFR_{ct}} \quad (1)$$

Furthermore, the current density of WSe_2 at relative high potential (U>0.2V) in Tafel curve is larger than $MoSe_2$ and $TaSe_2$, indicating a fast diffusion velocity of the redox couple, similar to Pt CE. This can be attributed to its larger pore diameter.

4.3 Photovoltaic performance of DSCs

Figure 6 shows the photocurrent density–voltage (J–V) curves of the DSCs fabricated using TMS-CEs and Pt-CE. The photovoltaic parameters of the DSCs are summarized in Table 1. As shown in Table 1, the DSCs based on TMS-CEs exhibit same V_{OC} (0.73 V), higher than that of the one with Pt-CE (0.70 V). This phenomenon could be attributed to the relative high R_s of selenide CEs that has revealed by the aforementioned EIS measurements according to literature.[13c,22] The DSCs based on three TMS-CEs have lower J_{SC}

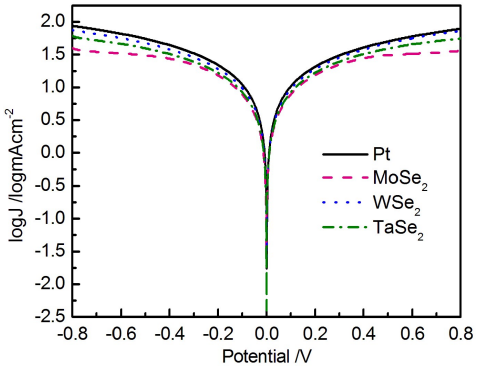

Figure 5 Tafel polarization curves of the symmetrical cells based on the various electrodes.

Table 1 EIS, CV, Tafel, and Photovoltaic performance parameters of the DSCs based TMSes and Pt

CEs	R_s/ Ωcm^2	R_{ct}/ Ωcm^2	CPE/μF	Z_N/ Ωcm^2	E_{pp}/ mV	J_0/ $mAcm^{-2}$	J_{lim}/ $mAcm^{-2}$	V_{OC}/ V	J_{SC}/ $mAcm^{-2}$	FF	PCE/%
Pt	6.32	1.32	42.2	1.21	140	5.62	80.19	0.70	16.84	0.67	7.91
$MoSe_2$	10.32	2.43	147.0	3.81	120	1.86	39.80	0.73	14.11	0.65	6.70
WSe_2	10.70	0.78	134.0	1.15	60	4.87	75.32	0.73	15.50	0.66	7.48
$TaSe_2$	10.00	1.89	94.8	6.18	110	2.47	60.31	0.73	15.81	0.64	7.32

than that from the one based on Pt-CE. The higher total internal series resistance and the increased Nernst diffusion impedance of TMS-CEs derived from the thick catalyst layer might be responsible for it, which is also consistent with the aforementioned EIS measurements.[23] The DSCs based on $TaSe_2$ and WSe_2 have larger J_{SC} than $MoSe_2$. The photocurrent of DSCs may be affected by many factors, including electrical conductivity, electrocatalytic activity, electrolyte diffusion, etc. $TaSe_2$ has good electrical conductivity as shown in EIS, conductivity experiments, and subsequent energy band calculation results. This is conducive to the charge transfer, which leads to higher J_{SC}. WSe_2 has good catalytic activity and larger pore which in favor of catalytic regeneration and mass transfer of I_3^-. But its conductivity is slightly worse, which lead to a slightly lower J_{SC} than $TaSe_2$. The lowest J_{SC} was obtained for $MoSe_2$ CE because of its worst catalytic activity and inferior ability for donating electron confirmed by the subsequent calculation.[24] The good catalytic activity of WSe_2 resulted in the largest FF, thus obtain higher conversion efficiency. For the DSCs based on $TaSe_2$ and WSe_2, PCEs of 7.32% and 7.48% were obtained, respectively, compared with that using Pt-CE (7.91%). Finally, a lower V_{OC} and J_{SC} were observed for the device with $MoSe_2$ CE, in which a lower PCE of 6.70% was obtained.

4.4 Theoretical investigation

The abnormal catalytic activity of $MoSe_2$ CE prompted us to explore by the density functional theory (DFT). Firstly, we calculate their band structure and the results are shown in Figure S6. The $MoSe_2$ and WSe_2 show a bandgap of 1.33 and 1.51eV, respectively. Interestingly, although profile of the band structure of $TaSe_2$ is similar to that of $MoSe_2$ or WSe_2, $TaSe_2$ shows metallicity because its Fermi level is through some band. Thus, the bulk resistance of $TaSe_2$ is smaller than those of $MoSe_2$ and WSe_2 and may be used to interpret the fact that the corresponding CE showed smaller R_s in EIS measurements.

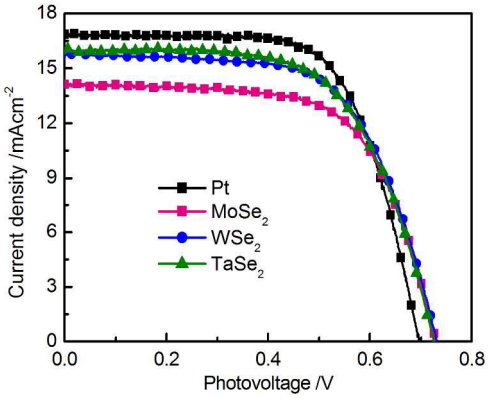

Figure 6 Photocurrent–voltage (J-V) curves of the DSCs based on three TMSes and Pt CEs, measured under simulated sunlight illumination condition (Xe arc lamp, 1.5 AM, 100 mW cm^{-2}).

Although possessed similar crystal structures, morphology, and band structure, $MoSe_2$ and WSe_2 exhibit obvious differences in electrocatalytic properties in the experiment. To further explore the origin of the catalytic activity differences for $MoSe_2$ and WSe_2, we calculated the adsorption process of the I_3^-/I^- redox couple on the surface of $MoSe_2$ (001) and WSe_2 (001). The molecular I_3 complex is considered for calculations in this study, given the charge neutrality in typical DFT calculations.[25] I^- is then generated from the induced bond elongation by extracting charges from the CE in the decomposition of molecular I_3 into three ions. To determine the energetically preferred adsorption, the molecular I_3 complex was placed initially on different sites, e.g., top, bridge, and hollow. Figure 7 shows the structures of I_3 and its adsorption on $MoSe_2$ (001) and WSe_2 (001) surface, and the corresponding projected density of states (PDOS). The results indicate that the I_3 complex is preferentially adsorbed at the top of Se on the $MoSe_2$ (001) surface and the hollow of WSe_2 (001) surface. When only I_3 complex is optimized, the I_1–I_2 bond is 2.86 Å. The I_1–I_2 bond can be elongated to 2.88 Å for the WSe_2 (001) surface and was shortened to 2.76 Å for the $MoSe_2$ (001) surface. The variation of I_1–I_2 bond length indicated that the dissociation of I_3 complex on the WSe_2 (001) surface is more conducive than the $MoSe_2$ (001) surface. Bader charge analysis suggests that the I_3 complex gains approximately 0.14e from the WSe_2 (001) surface but only 0.11e from the $MoSe_2$ (001) surface. Thus, the WSe_2 nanoparticles are more efficient in regenerating I_3^-/I^- redox couples in DSCs than the $MoSe_2$ nanoparticles. The theoretical calculation results agree well with the experimental data for the two CEs.

We further analyzed the projected density of states (PDOS) diagram for the I_3^- $MoSe_2$ and I_3^- WSe_2 in the configuration as shown in Figure 7d and e. From the PDOS diagram, the I 5p orbital, W and Mo d orbital, and Se 4p orbital exists obvious hybridization,

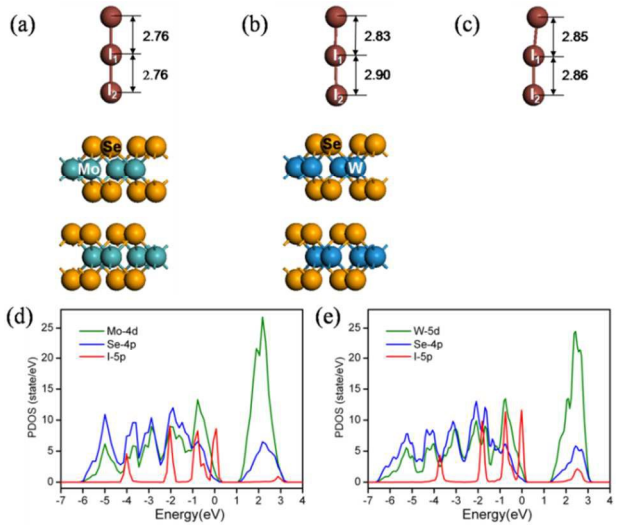

Figure 7 Side views of I_3 complex adsorption on (a) $MoSe_2$ (001) and (b) WSe_2 (001) surfaces, (c) the optimized I_3 complex, and projected density of states (PDOS) for I_3 complex adsorption on (d) $MoSe_2$ (001), (e) WSe_2 (001) surfaces. The Fermi energy is at 0 eV.

indicating the relatively large binding energy of I_3 complex adsorbed on WSe_2 (001) or $MoSe_2$ (001). When I_3 complex adsorbed on WSe_2 (001) surfaces, around Fermi level, I 5p electrons present five obvious isolated peaks, and there is a very complete overlapping with W5d and Se4p state at -0.8 eV. Meanwhile, a slight weak overlapping exists at around 2.5 eV. For $MoSe_2$, the overlapping at the -0.8 eV is significantly poor, and no obvious overlapping at 2.5 eV. Considering the above results, WSe_2 (001) surface is more conducive to the adsorption of I_3 complex than $MoSe_2$ (001) surface.

Thus, the WSe_2 nanoparticles are more efficient in regenerating of I_3^-/I^- redox couples in DSCs than the $MoSe_2$ nanoparticles, and then exhibit the superior catalytic activity. The theoretical calculation results agree well with the experimental data for the two CEs. To further research the difference of electrocatalytic activity, we calculated the ionization energy (IP) of WSe_2 and $MoSe_2$. As is well known, at the CE surface, where the electrons flow through the CE to the electrolyte, the main process is the reduction of electron acceptors in the electrolyte, which can be presented as: I_3^- (sol) + $2e^- \rightarrow 3I^-$ (sol). Therefore, if the CE material can easily yield electrons to the redox species in the electrolyte, the CE catalyticperformance can be significantly improved. According to Koopman's theorem,[26] IP for a semiconductor is approximately equal to the negative valence-band maximum (VBM) energy when the vacuum level is set as the zero of energy. IP is calculated using Equation 2, where E_{VBM} is the energy of VBM and E_0 is the vacuum level. The vacuum level and band structure of $MoSe_2$ (001) and WSe_2 (001) surface are calculated using DFT (Figure S7). The VBM energies of $MoSe_2$ (001) and WSe_2 (001) are -0.50 and -0.47 eV; the vacuum levels are 5.14 eV and 4.85 eV; thus, the corresponding IPs of $MoSe_2$ (001) and WSe_2 (001) are 5.64 eV and 5.32 eV, respectively (Figure S7). Compared with WSe_2, the IP of $MoSe_2$ is obviously higher, suggesting the inferior ability for donating electron of $MoSe_2$. The result is completely consistent with the preceding analysis. Thus, considering the dissociation of I_3 complex and electron donating ability, WSe_2 has better electrocatalytic activity than $MoSe_2$. The reason caused the bad electronic ability for $MoSe_2$ CE needs to be further studied.

$$IP = E_0 - E_{VBM} \quad (2)$$

4 Conclusions

In summary, we selected three metal elements with different outer electronic structure as our research object, and compared the catalytic activities of three targeted TMSs with similar crystal structures, through experimental validation and DFT computation. Our experiment suggests that these non-precious selenide materials exhibited different electrocatalytic activity in reduction of I_3^- and WSe_2 displayed the best electrocatalytic activity among three samples. DSCs with WSe_2-based CE achieved high PCE comparable to that of the one based on sputtered Pt-CE. Our computational results suggested that the bond length of I-I in the I_3 complex was elongated on the WSe_2 (001) surface. The hybridization of I5p orbital and WSe_2 surface was stronger than $MoSe_2$, which is conducive to the charge transfer from TMSs to I_3^-. These results indicated that the catalyst's composition and electronic structure have great influence on the catalytic activity. This work may provide a theoretical basis for the development of effective non-Pt catalysts and research of catalytic mechanism in the future.

Acknowledgements

Financial support provided by the National Natural Science Foundation of China (Grant No. 51402036, 51273032 and 91333104), International Science & Technology Cooperation Program of China (Grant No. 2013DFA51000), the Fundamental Research Funds for the Central Universities (Grant No. DUT15YQ109), and Natural Science Foundation of Anhui Province (Grant No. KJ2013A079). This research was also supported by the State Key Laboratory of Fine Chemicals of China.

Notes and references

[a] State Key laboratory of Fine Chemicals, School of Chemistry, Dalian University of Technology, Dalian, 116024, P. R. China.
E-mail: tinglima@dlut.edu.cn; shiyantao@dlut.edu.cn
[b]College of Chemistry and Materials Engineering, Anhui Science and Technology University, Fengyang, Anhui, 233100, P. R. China.
[c]School Petroleum and Chemical Engineering, Dalian University of Technology, Panjin Campus, Panjin 124221, P. R. China
[d]Graduate School of Life Science and Systems Engineering Kyushu Institute of Technology, Kitakyushu, Fukuoka, 808-0196, Japan

† Electronic Supplementary Information (ESI) available: XRD and diffractogram peaks assignment of selenides, Low-magnification SEM and HRTEM images of selenides. *J-V* curves of CE/CE devices for different TMSs. consecutive CVs of three TMS-based CEs, Band structures of the three TMSes. See DOI: 10.1039/b000000x/

‡ JiahaoGuo and Suxia Liang contributed equally to this work.

[1] Brian O'Regan, M. Grätzel, *Nature*, **1991**, *353*, 737-740.
[2] (a) A. Kay, M. Grätzel, *Sol. Energy Mater. Sol. Cells*, **1996**, *44*, 99-117; (b) F. Gao, Y. Wang, D. Shi, J. Zhang, M. Wang, X. Jing, R. Humphry-Baker, P. Wang, S. M. Zakeeruddin, M. Grätzel, *J. Am. Chem. Soc.* **2008**, *130*, 10720-10728; (c) A. Yella, C.L. Mai,S. M. Zakeeruddin, S.N. Chang, C. H. Hsieh, C. Y. Yeh, M. Grätzel,*Angew. Chem.* **2014**, *126*, 3017-3021.
[3] N. Papageorgiou, *Coord. Chem. Rev.* **2004**, *248*, 1421-1446.
[4] (a) H. W. Zhou, Y. T. Shi, Q. S. Dong, Y. X. Wang, C. Zhu, L. Wang, N. Wang, Y. Wei, S. Y. Tao, T. L. Ma, *J. Mater. Chem. A,* **2014**, *2*, 4347-4354; (b) S. N. Yun, H. W. Zhou, L. Wang, H. Zhang, T. L. Ma, *J. Mater. Chem. A,* **2013**, *1*, 1341-1348; (c) S. N. Yun, L. Wang, W. Guo, T. L. Ma, *Electrochemistry Communication*, **2012**, *24*, 69-73; (d) X. Lin, M. X. Wu, Y. D. Wang, A. Hagfeldt, T. L. Ma, *Chem. Commun.*,**2011**,*47*, 11489-11491; (e) M. X. Wu, X. Lin, L. Wang, W. Guo,Y. D. Wang, J. Q, Xiao, A. Hagfeldt, T. L. Ma, *J. Phys. Chem. C*, **2011**, *115*, 22598-22602.
[5] (a) M. X. Wu, Q. Y. Zhang, J. Q. Xiao, C. Y. Ma, X. Lin, C. Y. Miao, Y. J. He, Y. R. Gao, A. Hagfeldt, T. L. Ma, *J. Mater. Chem.*, **2011**, *21*, 10761-10766; (b) Y. D. Wang, M. X. Wu, X. Lin, Z. C. Shi, A. Hagfeldt, T. L. Ma, *J. Mater. Chem.*, **2012**, *22*, 4009-4014; (c) S. N. Yun, M. X. Wu, Y. D. Wang, J.Shi, X.Lin, A.Hagfeldt, T.L. Ma, *ChemSusChem*,**2013**, *6*,411-416;
[6] (a) M. X. Wu, T. L. Ma, *ChemSusChem*, **2012**, *5*, 1343-1357; (b) M. X. Wu, X.Lin, A.Hagfeldt, T. L. Ma, *Angew. Chem. Int. Ed.,***2011**, *50*, 3520-3524; (c) M. X. Wu, X. Lin, Y. D. Wang, W. Guo, D. D. Qi, X. Peng, A. Hagfeldt, M. Gratzel, T. L. Ma, *J. Am. Chem. Soc.*,**2012**, *134*, 3419-3428; (d) S. N. Yun, L. Wang, C. Y. Zhao, Y. D. Wang, T. L. Ma, *Phys. Chem. Chem. Phys.,***2013**, *28*, 4286-4290;
[7] M. X. Wu, Y. D. Wang, X. Lin, N. S. Yu, L. Wang, L. L. Wang, A. Hagfeldt, T. L. Ma, *Phys. Chem. Chem. Phys.*,**2011**,*13*, 19298-19301.
[8] M. X. Wu, J. Bai, Y. D. Wang, A. Q. Wang, X. Lin, L. Wang, Y. Shen, Z. Wang, A. Hagfeldt, T. L. Ma, *J. Mater. Chem.,* **2012**, *22*, 11121-11127.
[9] J. H. Guo, Y. T. Shi, Y. T. Chu, T. L. Ma, *Chem. Commun.*, **2013**, *49*, 10157-10159.
[10] (a) W. U. Huynh, J. J. Dittmer, A. P. Alivisatos, *Science*, **2002**,*295*, 2425-2427; (b) X. Peng, L. Manna, W. Yang, J. Wickham, E. Scher, A.

P. Kadavanich, A. P. Alivisatos, *Nature*, **2000**, *404*,59-61; (c) Y. Hu, J. F. Chen, W. M. Chen, *Materials Letters,* **2004**, *58*, 2911-2913; (d) X. Zhang, Z. Liu, Q. Li, Y. Leung, K. I. S. Hark, *Adv. Mater.,* **2005**, *17*, 1405-1412; (e) Q. Peng, Y. Dong, Z. Deng, X. Sun, Y. D. Li, *Inorg. Chem.*, **2001,** *40*, 3840-3841.

[11] (a) Z. Meng, Y. Peng, L. Xu, W. Yu, Y. Qian, *Chem. Lett.,* **2001,** *30*, 776-779; (b) L. Li, Z. Chen, Y. Hu, X. Wang, T. Zhang, W. Chen, Q. Wang, *J. Am. Chem. Soc.,* **2013**, *135*, 1213-1216; (c) Matthew A. Franzman, Cody W. Schlenker, Mark E. Thompson, Richard L. Brutchey, *J. Am. Chem. Soc.,* **2010**, *132*, 4060-4061.

[12] (a) L. F. Zhang, C. Y. Zhang, *Nanoscale*, **2014**, *6*, 1782-1789; (b) M. R. Gao, Q. Gao, J. Jiang, C. H. Cui, W. T. Yao, S. H. Yu, *Angew. Chem.Int. Ed.,* **2011**, *123*, 5007-5010; (c) Y. J. Feng, T. He, N. Alonso-Vante, *Fuel Cells*, **2010**,*10*, 77-83; (d) M. R. Gao, S. Liu, J. Jiang, C. H. Cui, W. T. Yao, S. H. Yu. *J. Mater. Chem.,* **2010**, *20*, 9355-9361; (e) Y. J. Feng, N. Alonso-Vante, *Electrochimica Acta,* **2012**,*72*,129-133.

[13] (a) F. Gong, H. Wang, X. Xu, G. Zhou, Z. S. Wang, *J. Am. Chem. Soc.,* **2012**, *134*, 10953-10958; (b) F. Gong, X. Xu, Z. Q. Li, G. Zhou, Z. S. Wang, *Chem. Commun.*, **2013**, *49*, 1437-1439; (c) J. H. Guo, Y. T. Shi, C. Zhu, L. Wang, N. Wang, T. L. Ma, *J. Mater. Chem. A,* **2013**, *1*, 11874-11897; (d) Z. Zhang, S .Pang, H. Xu, Z.Yang, X. Zhang, Z. Liu, X. Wang, X. Zhou, S. Dong, X. Chen, L. Gu, G. Cui, *RSC Advanced,* **2013**, *3*, 16528-16533.

[14] X. M. Fang, T. L. Ma, G. Guan, M. Akiyama, E. Abe, *J. Photochem. Photobiol. A,* **2004**, *164*, 179-182.

[15] G.Kresse, & J. Hafner, *Phys. Rev. B.*, 1994,**49**,14251.

[16] G.Kresse, & J.Furthmuller, *Comput. Mater. Sci.*, 1996,**6**,15.

[17] G. Kresse, & J. Furthmuller, *Phys. Rev. B*,1996,**54**,11169.

[18] P. E.Blöchl, *Phys. Rev. B*,1994,**50**,17953.

[19] Seholz Fritz., *Springer-Verlag Berlin Heidelberg*, **2010**, pp. 19-35.

[20] G. R. Li, F. Wang, Q. W. Jiang, X. P. Gao, P. W. Shen, *Angew.Chem. Int. Ed.*, **2010,** *49*, 3653-3656.

[21] M. Xu, Y. Rong, Z. Ku, A. Mei, X. Li and H. Han, *J. Phys. Chem. C,* **2013**, *117*, 22492.

[22] L. Yi, Y. Liu, N. Yang, Z. Tang, H. Zhao, G. Ma, Z. Su, D. Wang, *Energy Environ. Sci.,* **2013**, *6*, 835-840.

[23] R. Jia, J. Chen, J. Zhao, J. Zheng, C. Song, L. Lia and Z. Zhu, *J. Mater. Chem.*, **2010**, *20*, 10829-10834.

[24] C. H. Yoon, R. Vittal, J. Lee, W. S. Chae, K. J. Kim, *Electrochim. Acta,* **2008**, *53*, 2890-2896.

[25] (a) Y. C. Wang, D. Y. Wang, Y. T. Jiang, H. A. Chen, C. C. Chen, K. C. Ho, H. L. Chou, C. W. Chen, *Angew. Chem. Int. Ed.,* **2013**, *125*, 6826-6830; (b) S.N. Yun, H. Zhang , H.H. Pu , J.H. Chen, A. Hagfeldt, T. L. Ma, *Adv. Energy Mater.,* **2013**,*11,* 1407-1412.

[26] Dennis P. Piet, David Danovich, Han Zuilhof, Ernst J. R. Sudhölter. *J. Chem. Soc., Perkin Trans.,***1999**, *2*, 1653-1658.